



Strain-Rate Effects on the Crack Evolution Pattern and Damage Characteristics of Cemented Paste Backfill

Kang Zhao · Yun Zhou · Xiang Yu · Yajing Yan · Zhiwei He · Pengfei Shan · Xiangwei Zhang · Yongbo Ji

Received: 10 August 2021 / Accepted: 24 June 2022 / Published online: 26 August 2022
© The Author(s), under exclusive licence to Springer Nature Switzerland AG 2022

Abstract Because the damage to cemented paste backfill (CPB) caused by orebody retrieval can be approximated as a loading process under different strain-rates, studying the sprouting and expansion patterns of microcracks in CPB under uniaxial compression to predict and evaluate fracture damage to CPB is essential. In this study, uniaxial compression tests, simultaneous acoustic emission, and digital image correlation monitoring tests of CPB under four strain-rates were conducted in a laboratory. Based on the principles of energy dissipation and damage mechanics, the energy consumption values of the CPB at different strain-rates were calculated, and the energy damage evolution process of the CPB damaged by compression was explored. The

results show that (a) unlike high-strength rocks, CPB exhibits a critical strain-rate phenomenon, and when the strain-rate exceeds the critical value, the strength of CPB decreases with an increasing strain-rate. (b) As the strain-rate increases, the energy accumulated within the specimen cannot be effectively released, and the energy tends to accumulate in one part of the specimen. (c) The damage evolution curves of CPB at different strain-rate are all “S”-shaped and can be divided into phases of slow-growth damage, damage stabilization and accelerated growth, and damage growth rate slowdown. This study illustrates the damage evolution process of CPB under loading, which can be used in the study of CPB damage behavior resulting from orebody retrieval.

K. Zhao · Y. Zhou · Y. Yan
Solids Waste and Chemicals Management Center, Ministry of Ecology and Environment, Beijing 100029, China

K. Zhao · Y. Zhou · X. Yu · Z. He · X. Zhang · Y. Ji
School of Civil and Surveying & Mapping Engineering, Jiangxi University of Science and Technology, Ganzhou 341000, Jiangxi, China

Y. Zhou (✉)
School of Civil and Resources Engineering, University of Science and Technology Beijing, Beijing 100083, China
e-mail: zhouyun2816@163.com

P. Shan
State Key Laboratory of Coal Resources in Western China, Xi'an University of Science and Technology, Xi'an 710054, China

Keywords Cemented paste backfill · Crack evolution · Damage characteristics · Strain-rate · Digital image correlation

1 Introduction

CPB are usually prepared by mixing tailings, cement, and water at a specific ratio (Qi and Fourie 2019; Argane et al. 2015), and their strength and mechanical properties are influenced by particle gradation and proportioning along with slurry concentration, type of cementing agent, age of maintenance, and composition of the material (Chen et al. 2017; Liu et al. 2020a; Zhao et al. 2020a; Carabba et al. 2019; Qi

et al. 2018a; Sun et al. 2019). In recent years, mining scholars have conducted many studies on the strength and mechanical properties of CPB (Zhao et al. 2022; Fu et al. 2020; Zhang et al. 2020; He et al. 2021; Zhou et al. 2020, 2021; Das and Leung 2019). Felekoğlu et al. 2009 investigated the effects of fiber type and matrix structure on the mechanical properties of self-compacting microconcrete composites, and Liu et al. 2020b investigated the mechanical, hydration, microstructural, and electrical properties of CPB and derived key factors for the strength of CPB. Xu et al. 2013) obtained microscopic patterns of colloidal rock formation of ultrafine whole tailings sand materials under different conditions using X-ray diffraction (XRD) energy spectrum analysis and electron microscopy scanning methods. Cao et al. 2020 investigated the internal cracking mechanism and strength behavior of cement-fiber-tailings matrix composites using industrial CT and found that the damage to the specimens was mainly in the form of tensile, shear, and mixed tensile/shear damage with high strength values and large crack volumes. Xue et al. 2019a, 2019b investigated the mechanical, flexural, and microstructural properties of CPB. Dzaye et al. 2020 monitored the early acoustic emission (AE) of cement and fly ash slurries and found that the high sensitivity of AE made it possible to record elastic waves within the cementitious material and to detect even low-intensity activity. The results of the aforementioned studies reveal that the current research on the strength of CPB has mainly focused on cementitious materials and the composition of tailings materials. Few reports have been conducted on the effects of strain-rate changes on the crack evolution patterns and damage characteristics of CPB.

The results of numerous studies have shown that changes in the strain-rate can have significant effects on the mechanical properties of materials (Rosenthal et al. 2017; Mahanta et al. 2017; Cao et al. 2019; Zhao et al. 2020b; Gilat et al. 2007; Comley and Fleck 2012; Lee et al. 2012; Xia et al. 2015). Thomson et al. 2017 investigated the effect of the strain-rate on the fracture angle of inter-fiber failure (IFF) using a new effective Puck criterion and showed that the ability to predict the direction of the fracture face was improved at high strain-rates. Zhu et al. 2015 conducted dynamic Brazilian tests on rocks at medium strain-rates and showed that the dynamic indirect tensile strength of rocks increased with increasing

strain-rate. Stoddart et al. 2013 investigated a strain-rate based model of member connections and observed that strain-rate corrections to the model of jointed members could accurately model strain-rate induced hardening, and the reduction in damage rotation occurred in joints under dynamic conditions. The above studies demonstrate that strain-rate has a significant effect on the mechanical properties of materials. However, these studies have mainly focused on high-strength materials, such as rocks and metallic components, while few studies have been conducted on CPBs with lower strengths.

The main cause of deformation of CPB in mining production practice derives from unloading. In other words, the CPB changes from a stable three-way stress state to a state in which they lose their binding in a certain direction, and the deformation of the CPB increases further after unloading, where the characteristics are equivalent to loading under laboratory conditions. Therefore, the strain-rate studied in indoor tests can be reflected as the unloading rate (such as the orebody recovery rate) under field conditions. With a stage empty field followed by a filling mining method taken as examples, the orebody is divided into an ore house and ore pillar, in which the ore house is filled after back mining. The one-step CPB can be considered a cemented ore pillar, and the back-mining works of the two-step pillar are completed under the support of a one-step CPB. The one-step CPB creates effective operating conditions for the two-step pillar back-mining works (Zhao et al. 2021). The stress state of the CPB at the one-step mining site can be approximated as a three-way stress state, and the CPB is in an unloaded state when the adjacent two-step orebody is retrieved. Therefore, the damage to the CPB caused by the two-step orebody retrieval can be approximated as a loading process at different strain-rates (Zhao et al. 2021; Hou et al. 2020; Li et al. 2016). A reasonable strain-rate is first determined through indoor tests, and then the corresponding orebody recovery rate is converted to provide guidance for safe underground production.

This study reveals the intrinsic relationship between energy dissipation and strain and damage to CPB at different strain-rates by conducting uniaxial compression tests on CPB under different strain-rates. The deformation and damage law of CPB under different strain-rates is elaborated from an energy point of view, and the energy damage evolution process

of the compression damage to the CPB is revealed. The results of this study can provide a reference for exploring the damage mechanisms of CPB and ensuring safe production.

2 Experimental Design and Equipment

2.1 Experimental Materials

The materials used for the tests were whole tailings sand from a metal mine in Henan, China, composite silicate cement of P. C32.5, and tap water. After the whole tailings sand was dried, the particle size distribution of the tailings sand was determined by using a laser particle size analyzer. The data measured by the tests could then be analyzed to obtain

the cumulative distribution of tailings sand particle size as $d_{10}=0.43\ \mu\text{m}$, $d_{30}=1.28\ \mu\text{m}$, $d_{50}=3.15\ \mu\text{m}$, and $d_{60}=4.03\ \mu\text{m}$. The inhomogeneity coefficient of the tailings sand was $C_u=9.37$, and the curvature coefficient was $C_c=0.95$, showing that the test tailings sand was poorly graded. The results of the tailings sand particle size tests are shown in Fig. 1a. Figure 1b shows the XRD pattern of the tailings sand in this mine. Figure 1b shows that the minerals were mainly composed of quartz, calcite, and diopside, with other small amounts of gypsum and mica. The surface microarea morphologies of the CPB specimens were examined using an MLA650F field-emission scanning electron microscope (FEI, USA). The following parameters are assumed: the resolution is 30 nm, and the maximum acceleration voltage is 20 kV, as shown in Fig. 1c.

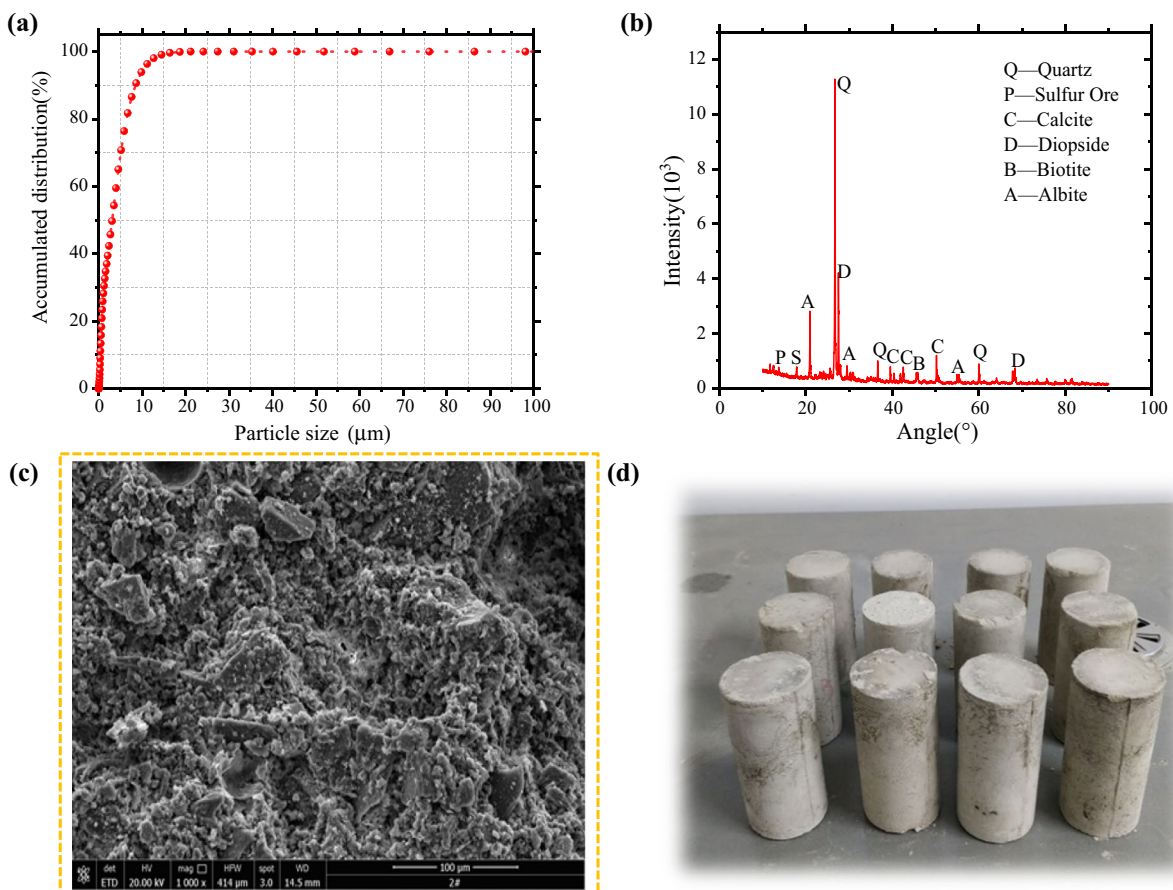


Fig. 1 Testing the mineral composition of CPB: **a** particle size distribution of tailings sand, **b** mineral composition of tailings, **c** fracture morphology characteristics of CPB specimens, **d** some CPB specimens

2.2 Specimen Production

The specimens were made in accordance with the requirements of the official version of JGJ 55–2011, “Ordinary Concrete Proportioning Design Regulations” (JGJ 55–2011 2011). A cylindrical mold with a diameter of 50 mm and height of 100 mm was used to fabricate the specimens. First, mine tailings sand, silicate cement, and tap water were prepared at a cement tailings ratio of 1:8 and mass fraction of 68%. Then, the material was mixed well and spoonfuls of filling slurry were poured into the cylindrical mold quickly and evenly according to the sequence. Finally, the surface of the test mold was smoothed following the initial setting of the slurry, and the mold was demolded after 24 h. To be more in line with actual engineering scenarios, the specimens were naturally maintained, and each specimen was weighed after the maintenance age reached 14 d. This was followed by uniaxial compression tests. Some specimens prepared for the tests are shown in Fig. 1d.

2.3 Test Methods and Equipment

2.3.1 Uniaxial Compressive Strength Test

The pressure machine equipment for the uniaxial compression tests of CPB was an MTS microcomputer-controlled electronic universal testing machine. The maximum output force of the MTS is 50 kN, and the accuracy and error of its test system are feasible in the uniaxial compressive strength test of CPB. Test loading was conducted under the displacement control mode, and the strain-rate of this test was divided into four gradients: $2 \times 10^{-5} \text{ s}^{-1}$, $4 \times 10^{-5} \text{ s}^{-1}$, $8 \times 10^{-5} \text{ s}^{-1}$, and $10 \times 10^{-5} \text{ s}^{-1}$. Four specimens were tested under each strain-rate, and the specimens with deviations of 20% or more were rejected. Additional specimens were tested, and the data of the most representative specimen were taken as the test data.

2.3.2 AE Test System

The AE equipment used for the tests was a Micro-II Express Digital AE System (Express-8 AE SYSTEM). The parameters of the AE test system are listed in Table 1.

Table 1 Parameters of AE test system

Sampling frequency	Wave-form threshold	Preamplifier gain	Interval parameter	Sampling points	Trigger mode
1024 kHz	35 DB	40 DB	50 μs	1024 kHz	Internal trigger

2.3.3 DIC Test System

Digital image correlation (DIC) is an optical measurement method based on non-contact images. Digital imaging equipment was first used to acquire scatter images of objects under different loads, where a correlation-based matching algorithm was then used for image analysis to extract information quantitatively on the full-field displacement and strain response of the structure (Golewski 2019; Reu et al. 2018; Dai et al. 2019) for full-field displacement and deformation measurements. DIC is widely used in the study of fracture processes in materials such as rock specimens because of its advantages of being non-contact, providing real-time dynamic measurements, and offering high-resolution imaging (Rokoš et al. 2018; Lacidogna et al. 2020; Yashar et al. 2017; Roux-Langlois et al. 2015; Kourkoulis et al. 2017; Pierron et al. 2011). The DIC test system used in the experiment mainly consists of a Canon EOS 700D camera with an image resolution of 18 megapixels, two sets of white LED light sources, a computer, and 2D-DIC analysis software. To maintain the camera shooting direction and ensure that the model surface remains perpendicular, the first level of the camera tripod must be used. The camera viewfinder electronic level is then used to maintain the camera level. The laser pointer is then mounted on the camera body, the glass mirror temporarily attached to the surface of the model is aligned, and the tripod is fine-tuned until the incident and reflected light coincide with each other. The camera is controlled by an infrared remote control for shooting, thus avoiding camera vibrations caused by manual operation. Two sets of LED light sources provide uniform and bright illumination of the model surface. Prior to the test, the camera was turned on to warm up for 20–30 min to ensure that it reached a thermally stable state to avoid distortion

of the acquisition map normally resulting from camera heat.

3 Analysis and Test Results

3.1 Peak Strength Characteristics of CPB

Figure 2 shows the stress–strain curves of CPB under uniaxial compression at various strain-rates. The stress–strain curves presented show that the uniaxial compression damage process of the CPB under different strain-rates mainly went through the compression-density, linear-elastic, yielding, and damage stages. However, the strain-rates were different, and the stress–strain curves of the CPB showed some variability.

The effects of the strain-rate on the linear elastic deformation phase of the stress–strain curve of the CPB were significant. When the strain-rate was in the range of $2 \times 10^{-5} \text{ s}^{-1}$ to $8 \times 10^{-5} \text{ s}^{-1}$, the linear elastic deformation of the CPB extended to higher levels as the strain-rate increased, and the peak stress also increased. When the strain-rate was in the range of $8 \times 10^{-5} \text{ s}^{-1}$ to $10 \times 10^{-5} \text{ s}^{-1}$, the extension level of the linear elastic deformation phase of the CPB tended to decrease as the strain-rate increased, and the peak stress was then reduced. From the peak stress variation law, it is clear that a critical strain-rate phenomenon occurs in low-strength CPB.

Figure 2 shows that the compressive strength of the CPB specimens tended to first increase and then

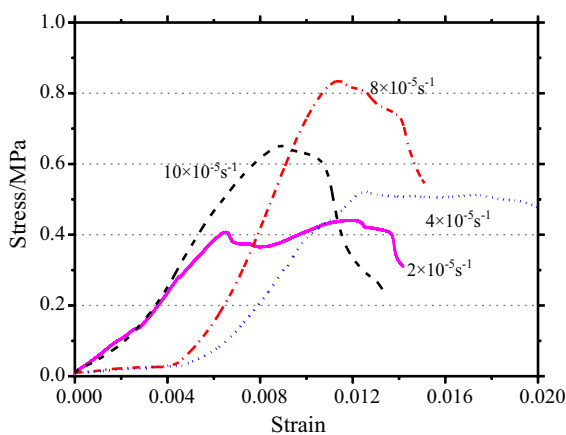


Fig. 2 Stress–strain curves of CPB under different strain-rates

decrease with an increase in the strain-rate, where the critical value of the strain-rate corresponding to the turning point of the strength change is called the critical strain-rate. A critical strain-rate of approximately $8 \times 10^{-5} \text{ s}^{-1}$ was observed for CPB specimens with a mass fraction of 68% and cement-tailings ratio of 1:8. When the strain-rate was lower or higher than $8 \times 10^{-5} \text{ s}^{-1}$, the strength of the CPB specimens increased or decreased, respectively, with an increase in the strain-rate. The strain-rate increased from $2 \times 10^{-5} \text{ s}^{-1}$ to $8 \times 10^{-5} \text{ s}^{-1}$, and the compressive strength of the CPB specimens increased from 0.441 to 0.837 MPa with a 90% increase in strength. The strain-rate increased from $8 \times 10^{-5} \text{ s}^{-1}$ to $10 \times 10^{-5} \text{ s}^{-1}$, which resulted in a 22% reduction in compressive strength compared with the maximum value. The CT ratio formulated in this test was 1:8, and the CPB with a mass fraction of 68% exhibited a critical strain-rate phenomenon, indicating the existence of a critical strain-rate characteristic of low-strength CPB.

The mechanism of the effect of the strain-rate on the mechanical properties of CPB could be attributed to the following two factors.

- (1) The preparation process of the CPB and the hardening process of water seepage, dry shrinkage, and heat of hydration of cement tended to cause initial defects such as air bubbles, holes, microcracks, and microporosity inside the CPB. This could thus be described in terms of fine defects within the CPB.
- ① The preparation process of the CPB and the hardening process of water seepage, dry shrinkage, and heat of hydration of cement tended to cause initial defects such as air bubbles, holes, microcracks, and microporosity inside the CPB. This could thus be described in terms of fine defects within the CPB.
- ② When the strain-rate was at a low level, the initial defects within the CPB had sufficient time to develop and evolve, thus resulting in a lower strength of the CPB. As the strain-rate increased, the initial defect development within the CPB was limited, and the degree of damage to the CPB decreased, thus increasing the CPB strength. This phenomenon was consistent with the variation patterns of hard and brittle rocks.

- ③ When the strain-rate exceeded the critical strain-rate, the stress concentration level at the defect continued to increase with additional increases in the strain-rate. This caused internal cracks of the CPB to extend, and thus, the CPB strength gradually decreased.
- (2) From an energy point of view, the uniaxial compression damage of the CPB at different strain-rates was essentially the result of the combined effect of energy dissipation and energy release (Hou et al. 2020). Differences in the mechanical properties of CPB could therefore be accounted for from an energy perspective.
 - ① When the strain-rate was in the critical strain-rate range, the total input energy increased as the strain-rate increased. This part of the energy was used to limit the development of microcracks inside the CPB, allowing the linear elastic deformation phase to extend to a higher level, thereby increasing the load-bearing capacity of the CPB.
 - ② When the strain-rate was greater than the critical strain-rate, the input energy continued to increase with the strain-rate, and the crack development time for the CPB was further reduced. At this time, most of the energy was stored in the solid load-bearing structure in the form of elastic strain energy. However, for the lower-strength CPB, the solid load-bearing structure tended to be the first to breakdown because of the higher internal elastic strain energy, which resulted in the reduction of the effective load-bearing area and in turn reduction of the load-bearing capacity of the CPB.

3.2 Fracture Mechanism and Crack Evolution Law of CPB Under Different Strain-rates

3.2.1 Strain Field Evolution Law of CPB at Different Strain-rates

In previous studies (Hagara et al. 2012; Featherston 2012; Crammond et al. 2013), a DIC method was used to observe the uniaxial compression damage process of CPB specimens at different strain-rates.

The evolution of the global deformation field on the specimen surface during the rupture process was observed using DIC to summarize the crack initiation, extension, and penetration patterns of the CPB under different strain-rates from a qualitative perspective. The crack strain field evolution during the rupture of a specimen could be qualitatively described, and its fracture type could be visually determined. Breaking through the limitations of the traditional empirical-based judgment of fracture types existing in CPB, this study thus helps to improve the understanding of the damage mechanisms of CPB.

Figure 3 shows strain field diagrams of CPB under different strain-rates. Because the DIC method can accurately record the strain and displacement of a specimen during the entire loading process, it is expected that the DIC method can explain the damage process of the specimen. Of the recorded test results, the strain test results of the specimen could reflect the location of the stress concentration in the specimen. Similarly, the development of the strain concentration could reflect the development process of cracks. The DIC strain test results at different strain-rates showed that the overall strain of each specimen was nonuniform and that an obvious strain concentration area existed, and this strain concentration area changed continuously with the loading process.

DIC analysis software was used in this study to analyze the scatter patterns collected during the tests and to reproduce the entire process of crack generation and expansion on the surface of the CPB specimens during test loading. The evolution of the strain field during damage to the CPB specimens better reflects the law of pore and crack expansion into macroscopic damage inside the specimens. The DIC observations reflect the shifting of the strain concentration zone during the loading process. The generation, extension, and evolution of cracks on the surface of the CPB specimens at different strain rates were also significantly different. Damage to the surfaces of the specimens at low strain rates tended to be in the form of tensile damage, with significant single-bevel shear damage occurring at high stress rates. Simultaneously, under strain-rate loading, the specimens were instantaneously released from the stress concentration when the peak strength was reached, and the rupture destabilization phenomenon was dramatic.

The red arrows in Fig. 3 indicate the transfer direction of the strain concentration. Experimental results

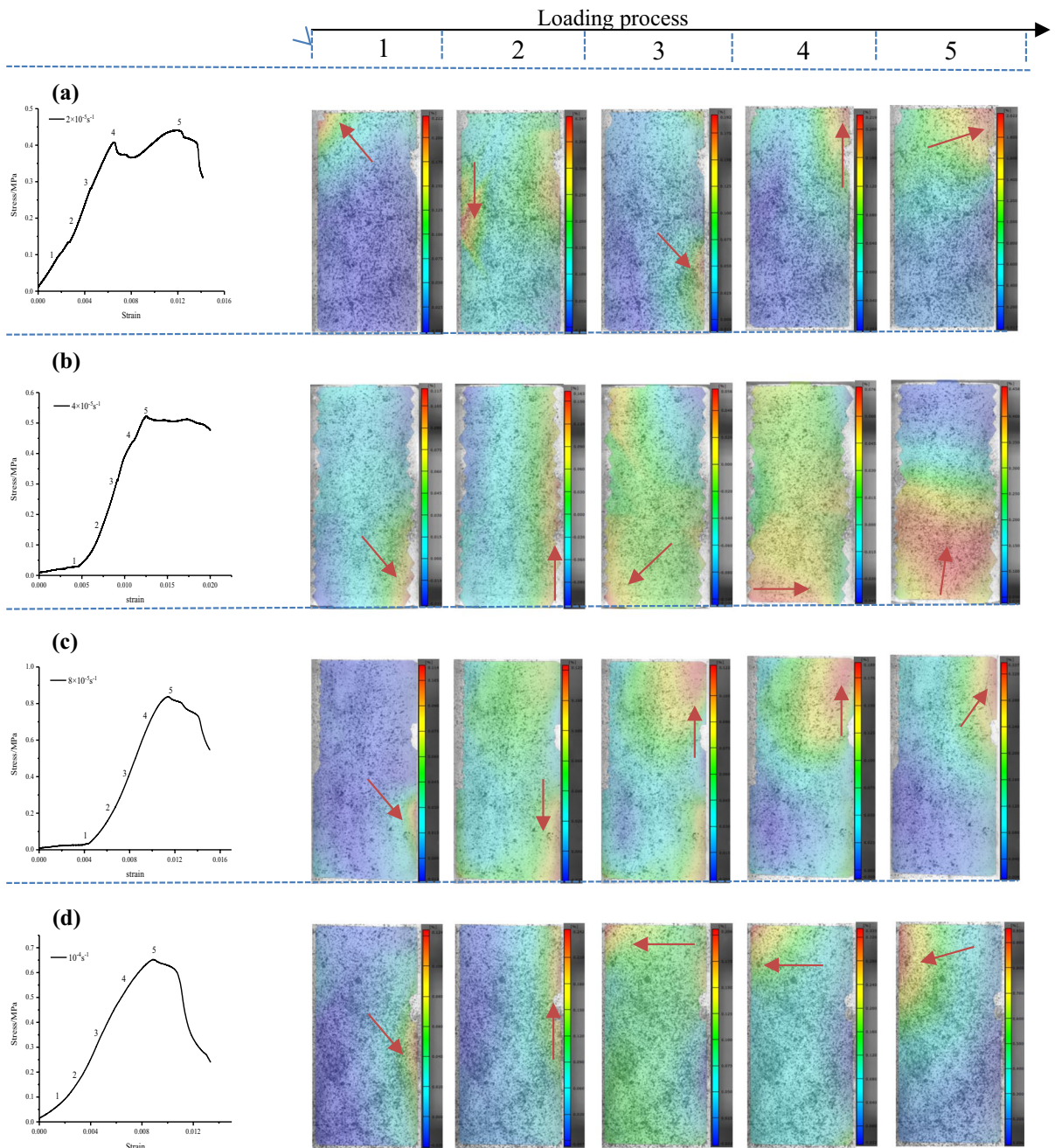
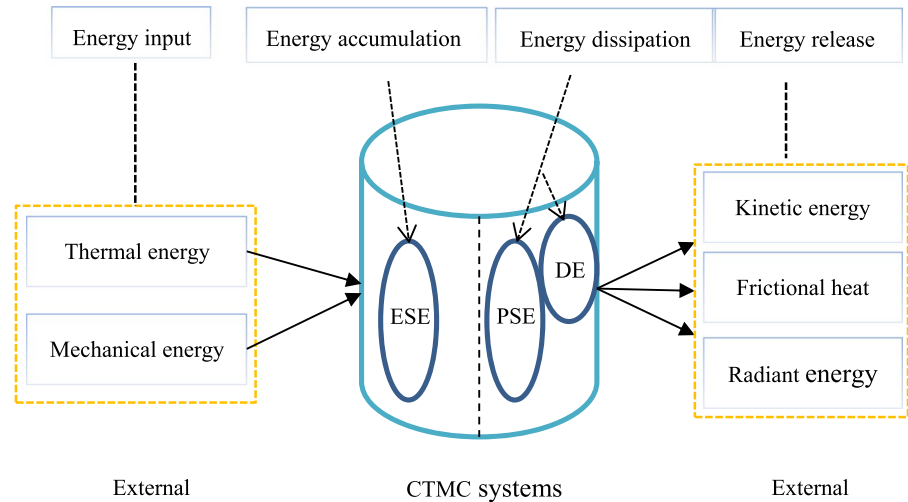


Fig. 3 Strain field distribution of CPB at different strain-rates **a** $2 \times 10^{-5} \text{ s}^{-1}$; **b** $4 \times 10^{-5} \text{ s}^{-1}$; **c** $8 \times 10^{-5} \text{ s}^{-1}$; **d** $10 \times 10^{-5} \text{ s}^{-1}$

revealed that the damage processes of CPB were different under different strain rates. Under a low strain rate ($2 \times 10^{-5} \text{ s}^{-1}$), the microcracks in the specimen could be fully extended during the loading process. The specimen had sufficient time for stress redistribution, and the accumulated energy could be fully

released. As the loading process continued, the specimen fractured along the primary crack and formed secondary cracks around the primary crack. When the strain rate increased to $4 \times 10^{-5} \text{ s}^{-1}$ and $8 \times 10^{-5} \text{ s}^{-1}$, the strain concentration zone of each specimen gradually developed from the specimen top to the bottom.

Fig. 4 Energy conversion of CPB with elastic strain energy (ESE), plastic strain energy (PSE), and damage energy (DE)



With a continuing increase in the strain rate, microcracks within the specimen could continue to develop. The development of microcracks was multidirectional and not unique. As the strain rate increased, the energy accumulated inside the specimen could not be released effectively, and the energy tended to accumulate in a certain part of the specimen ($8 \times 10^{-5} \text{ s}^{-1}$, $10 \times 10^{-5} \text{ s}^{-1}$: accumulation at the top of the specimen). In addition, the uniaxial compressive strength of the specimen was reduced because a higher strain rate caused a rapid release of considerable energy.

3.3 Energy and Energy Consumption Characteristics of CPB at Different Strain-rates

As CPB is a nonhomogeneous material, its mechanical properties show anisotropy and nonlinearity, and the deformation and damage processes are extremely complex and uncertain (Chen et al. 2018; Koupouli and Belem 2019; Cheng et al. 2019; Qi et al. 2018b; Yilmaz et al. 2013; Benzaazoua et al. 2004; Cihan-gir et al. 2015). Therefore, the strain-rate state as the basis for the strength of CPB may differ somewhat from the actual deformation damage law, where the strain-rate usually exhibits diversity and its strength is discrete. From thermodynamic theory, it can be concluded that energy absorption, transformation, and release occur with the external environment during deformation and damage to the CPB, and the final destabilization damage represents an energy-driven performance. Therefore, a study of the mechanical characteristics and essential features of the

deformation and damage to the CPB from an energy perspective is beneficial to reflect the damage law of the CPB in a more realistic manner.

3.3.1 Calculation of Energy During Loading

3.3.1.1 Energy Conversion Analysis As a nonhomogeneous individual, the CPB material has a variety of deformation modes during the process of loading, and energy conversion is conducted with the outside world using different energy forms. This energy conversion process is shown in Fig. 4.

The energy conversion process of the CPB system can be divided into four main parts: energy input, energy accumulation, energy dissipation, and energy release.

3.3.1.2 Calculation of the Loading Process Energy Consider a unit volume of a specimen deformed by an external force, where the physical process is assumed to have no heat exchange with the outside world; in other words, a closed system. Then, according to the first law of thermodynamics, we obtain

$$U = U^d + U^e \quad (1)$$

where U is the total energy input to the unit from external forces, U^d is the unit dissipation energy, U^e is the releasable elastic strain energy stored in the unit, and the U , U^d , and U^e units are measured in J/m^3 .

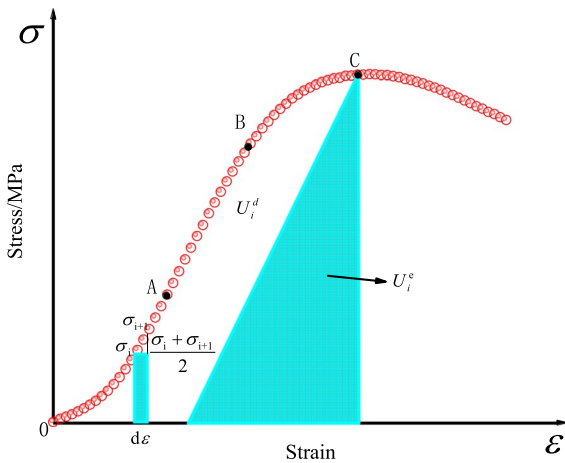


Fig. 5 Quantitative relationship between energy dissipation in unit volume and releasable dissipated energy

The strain-rate curve of the CPB unit is shown in Fig. 5. Here, U_i^d denotes the energy consumed before the peak, the shaded area U_i^e represents the strain energy stored in the specimen, and E_i is the unloaded modulus of elasticity.

The total input energy (U) resulting from the work done by the external force on the CPB can be considered the actual energy absorbed by the specimen (U_0). In this study, the energy calculation process was performed using a uniaxial compression formula. The energy absorbed by the specimen (U) could be obtained from the expression for each energy index in the principal stress space as given by Xie et al. 2005 and expressed as

$$U = \int \sigma_1 d\epsilon_1 = \sum_{i=0}^n \frac{1}{2} (\sigma_{i+1} + \sigma_i) (\epsilon_{i+1} - \epsilon_i) \quad (2)$$

where σ_i and ϵ_i are the stress and strain values, respectively, at any point on the axial stress–strain curve.

From (2), the total energy absorbed by the specimen (U) is the area of the stress–strain curve of the specimen down to the area of the transverse coordinate during the loading process. The released elastic strain energy (U^e) can be calculated using the elastic modulus E of the elastic section of the stress–strain curve instead of the unloaded elastic modulus E_i (Gong et al. 2022). The stress value at any point of the curve and the elastic modulus of the elastic segment can be used to calculate the releasable elastic strain energy at that point, that is.

$$U_i^e = \frac{\sigma_i^2}{2E} \quad (3)$$

where U_i^e and σ_i are the releasable strain energy and stress values at any point, respectively.

3.3.2 Strain-rate Effect on the Energy Evolution of CPB

The stress–strain curve characteristics determine how the compression, linear elastic, yielding, and failure stages are divided. In the entire deformation damage process, the energy evolution of the four stages has obviously different characteristics, which are described as follows: (1) Compression stage, in which the releasable elastic strain energy and dissipated strain energy accumulate simultaneously; (2) Linear elastic phase, in which the releasable elastic strain energy accumulates continuously, whereas the dissipative energy hardly increases; (3) Yielding stage, in which the increase in releasable elastic strain energy slows down, and energy dissipation is faster; (4) Failure phase, in which the elastic strain energy is released drastically, and the energy is drastically dissipated. However, the trend of energy evolution within the four stages does not change for different strain rates, which we analyze quantitatively as follows.

Figure 6 presents graphs for the total absorbed energy, released elastic strain energy, and dissipation energy and shows the stress–strain relationships of specimens for CPB at different strain rates. Figure 6 shows that the total energy tended to decrease and then increase with an increase in the strain rate. When the strain rate was in the range of $2 \times 10^{-5} \text{ s}^{-1}$ to $8 \times 10^{-5} \text{ s}^{-1}$, the total energy increased from 4548.75 to 5752.13 J/m³, a decrease of 26.46%. When the strain rate was in the range of $8 \times 10^{-5} \text{ s}^{-1}$ to $10 \times 10^{-5} \text{ s}^{-1}$, the total energy was reduced from 5752.13 to 4937.80 J/m³, a reduction of 14.16%. As the strain rate increased, the released elastic strain energy and dissipated energy before and after the peak, respectively, showed the same trend as the total energy, both first increasing and then decreasing.

The previous results reveal that the total energy, released elastic strain energy, and dissipation energy showed an overall increasing trend with increasing strain rate. The main reason for this was that as the strain rate increased, the far-field crack (which was

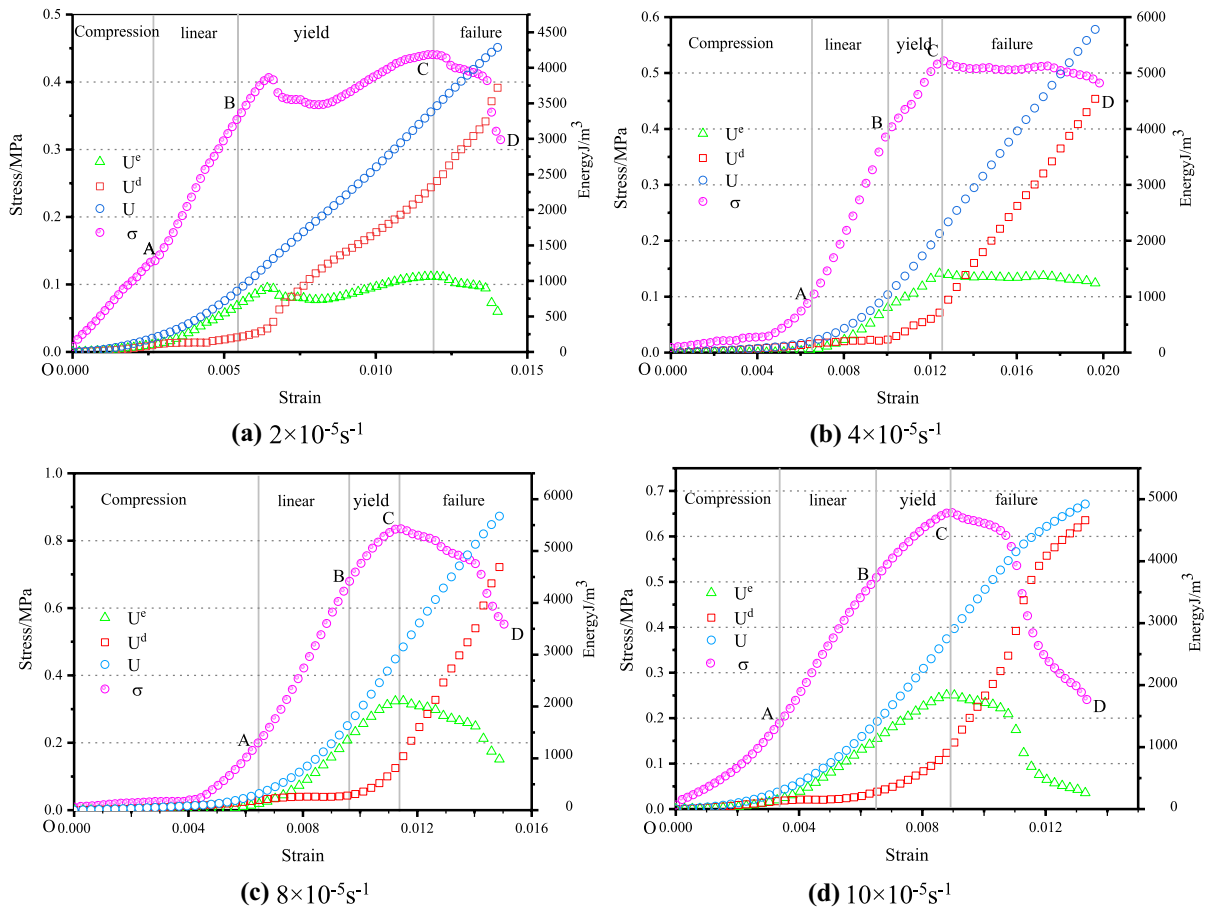


Fig. 6 Curve of energy evolution process of CPB

Table 2 Energy values of CPB under different strain-rates

Specimen number	Strain-rate s^{-1} (V)	Lg (V)	Pre-peak energy consumption	Post-peak energy consumption	Strain energy at peak stress	Total energy consumption
H-1	2×10^{-5}	- 4.7	643.3	3159.5	1064.9	3803.1
E-3	4×10^{-5}	- 4.4	880.1	3903.8	1830.4	4783.9
F-4	8×10^{-5}	- 4.1	938.8	3961	2119.0	4899.8
E-2	10×10^{-5}	- 4	901.6	3786.7	1849.9	4688.3

produced when the specimen was damaged) gradually increased, and the specimen generated a main crack that was gradually parallel to the direction of the axial force. The surface energy required for crack development in turn gradually increased (Lei et al. 2020).

Based on the aforementioned energy dissipation principle, the energy values can be calculated for the CPB at different stages of the uniaxial compression

stress–strain curve. The uniaxial compression energy values for the CPB at different strain rates are listed in Table 2.

Table 2 shows that when the strain rate of the CPB was $2 \times 10^{-5} \text{s}^{-1}$, the strain energy at which the peak stress was reached was 1064.9 J/m^3 . When the strain rate was increased to $4 \times 10^{-5} \text{s}^{-1}$, $8 \times 10^{-5} \text{s}^{-1}$, and $10 \times 10^{-5} \text{s}^{-1}$, the strain energy required for the

CPB specimens to reach the peak stress was 1830.4, 2119.0, and 1849.9 J/m³, respectively. As the strain rate increased, the strain energy required to reach the peak stress in the CPB tended to increase and then decrease. Within the critical strain-rate range, a positive correlation was found between the strain rate and strain energy at the peak stress, and beyond the critical strain-rate range, there was a negative correlation. When the strain rate increased from $2 \times 10^{-5} \text{ s}^{-1}$ to $10 \times 10^{-5} \text{ s}^{-1}$, the proportion of pre-peak energy to total energy consumption of the CPB was 16.92%, 18.40%, 19.16%, and 19.23%. This indicated that during uniaxial compression damage, with an increase in the strain rate, most of the energy was consumed in the postpeak rupture phase of the CPB, which intensified the postpeak damage deformation of the CPB.

In this test, the amount of prepeak energy consumption of the CPB tended to increase and then decrease with the strain rate, and the amount of pre-peak energy consumption increased with the strain rate in the critical strain rate range, indicating that an increasing amount of energy was consumed in the prepeak deformation phase of the CPB, improving the yield strength of the CPB. When the strain rate was greater than the critical strain rate value, the solid load-bearing structure was the first to break due to the higher internal strain energy as the total input energy increased. This resulted in lower energy consumption. Combining the experimental data in Table 2, the statistical regression analysis showed that the pre-peak energy consumption, postpeak energy consumption, strain energy at the peak stress, and total energy consumption of the CPB followed a quadratic function $Y = AX^2 + BX + C$ growth pattern with the logarithm of strain rate, where X is the logarithm of strain rate, A , B , and C are all test coefficients, and Y is the energy consumption value and strain energy. Figure 7 presents a curve showing the relationship between the energy consumption value and logarithm of the strain rate for the CPB.

Figure 8 shows that the energy consumption of the CPB tended to increase with an increase in axial strain. The energy consumption values of the CPB were basically similar to the axial compression strain relationship curves at different strain rates, and the main difference was that the energy consumption required to achieve the same axial deformation was significantly different in value.

Combined with the fitting results in Fig. 8, it can be seen that the growth of the energy consumption value of the CPB with respect to the axial strain generally followed the growth pattern of the logistic model ($Y = a + (b - a) / [1 + (\frac{x}{c})^p]$), where the parameters a , b , c , and p depend on the strain rate and other influencing factors, and x is the axial strain. The correlation coefficients of the model fits were all above 0.98, indicating a good overall fit (Hou et al. 2020).

3.4 Exploration of the Energy Damage Evolution Process for the Destruction of CPB

As previously mentioned, significant differences were observed in the energy consumption values of the CPB at different strain rates, whereas the yield damage and damage to the CPB were essentially the result of energy dissipation. Therefore, this study further investigated the damage mechanism of CPB under different strain rates and explored the connection between the energy dissipation characteristics and damage evolution of CPB. Explanations follow the damage intrinsic law of materials based on the principle of energy balance and the fundamental law of irreversible thermodynamics. When the process of damage to a specimen as the transformation of the structural phase into the damage phase is considered, additional work done by the external force due to the transformation of the structural phase in the specimen into the damage phase is defined as the damage dissipation energy, and this parameter is introduced into the energy balance equation of the specimen. Through analysis of the energy transformation of typical unitary bodies, the damage intrinsic model based on the energy method can be calculated, and a method to determine the damage dissipation energy is then provided. According to Zhou et al. (2014) regarding the damage dissipation energy model of geotechnical materials, the energy balance equation of the structural phase of the cementitious material specimen proposed in this study can be expressed as

$$\Omega dA_d = \frac{1}{2} A_n \sigma_n d\epsilon_n \tag{4}$$

where Ω is the damage dissipation energy of the specimen, σ_n is the stress in the structural phase, A_n is the area of the structural phase, and $d\epsilon_n$ is the microstrain that occurs in the structural phase when the damaged phase extends the microarea dA_d . In any

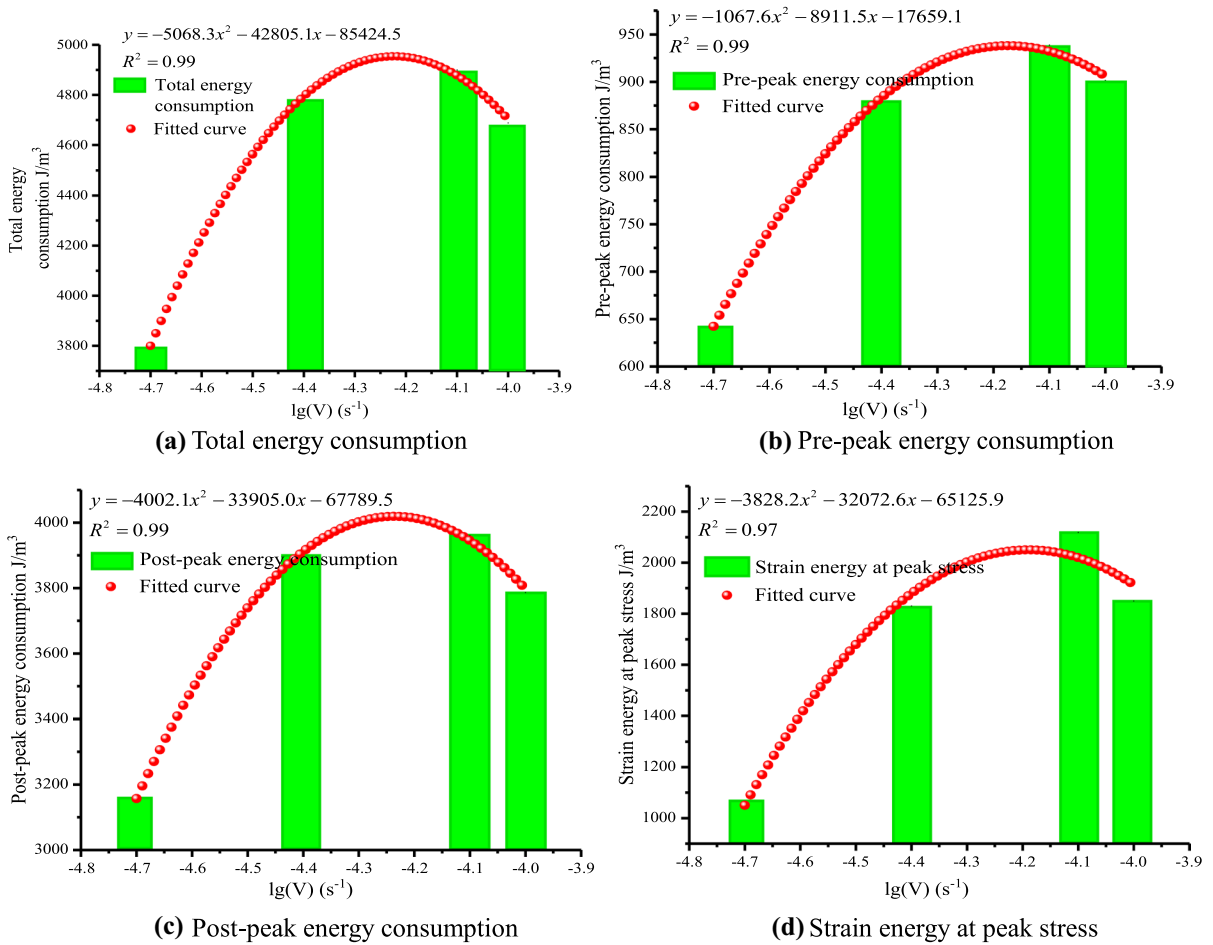


Fig. 7 Strain-rate effect curve of dissipated energy of CPB

cross-section, the damage variable is considered to be the ratio of the damage phase area (A_d) to the total cross-sectional area A as $D = A_d/A$. Therefore,

$$dD = \frac{1}{2\Omega}(1 - D)\sigma_n d\epsilon_n \tag{5}$$

When both ends of (5) are integrated and then the exponential transformation (considering the damage threshold) is performed, the expression for the damage variable can be determined by

$$D = \begin{cases} 0 & \epsilon \leq \gamma \\ 1 - \exp\left[-\frac{1}{2\Omega} \int \sigma_n d\epsilon_n\right] & \epsilon > \gamma \end{cases} \tag{6}$$

where γ is the damage threshold strain, taken as 0.4 ϵ_c , and ϵ_c is the corresponding strain at the peak stress.

For the integral calculation, the relationship of $\sigma_n - \epsilon_n$ can be derived using polynomial, exponential, rational fractional, and other models. In this study, the SIR model recommended in Griffiths et al. (2000) was used for the derivation. The SIR model can reflect the dynamic evolution of the internal structure and its own properties of the system with different components under the action of external forces. It can also simulate the damage and destruction process of concrete materials, giving the model the advantages of being smooth and continuous and having high fitting. This can be expressed as

$$y = c(e^{bx} - e^{ax}) \tag{7}$$

where $x = \epsilon/\epsilon_c$ denotes the ratio of strain to peak strain, $y = \sigma/\sigma_c$ denotes the ratio of stress to peak

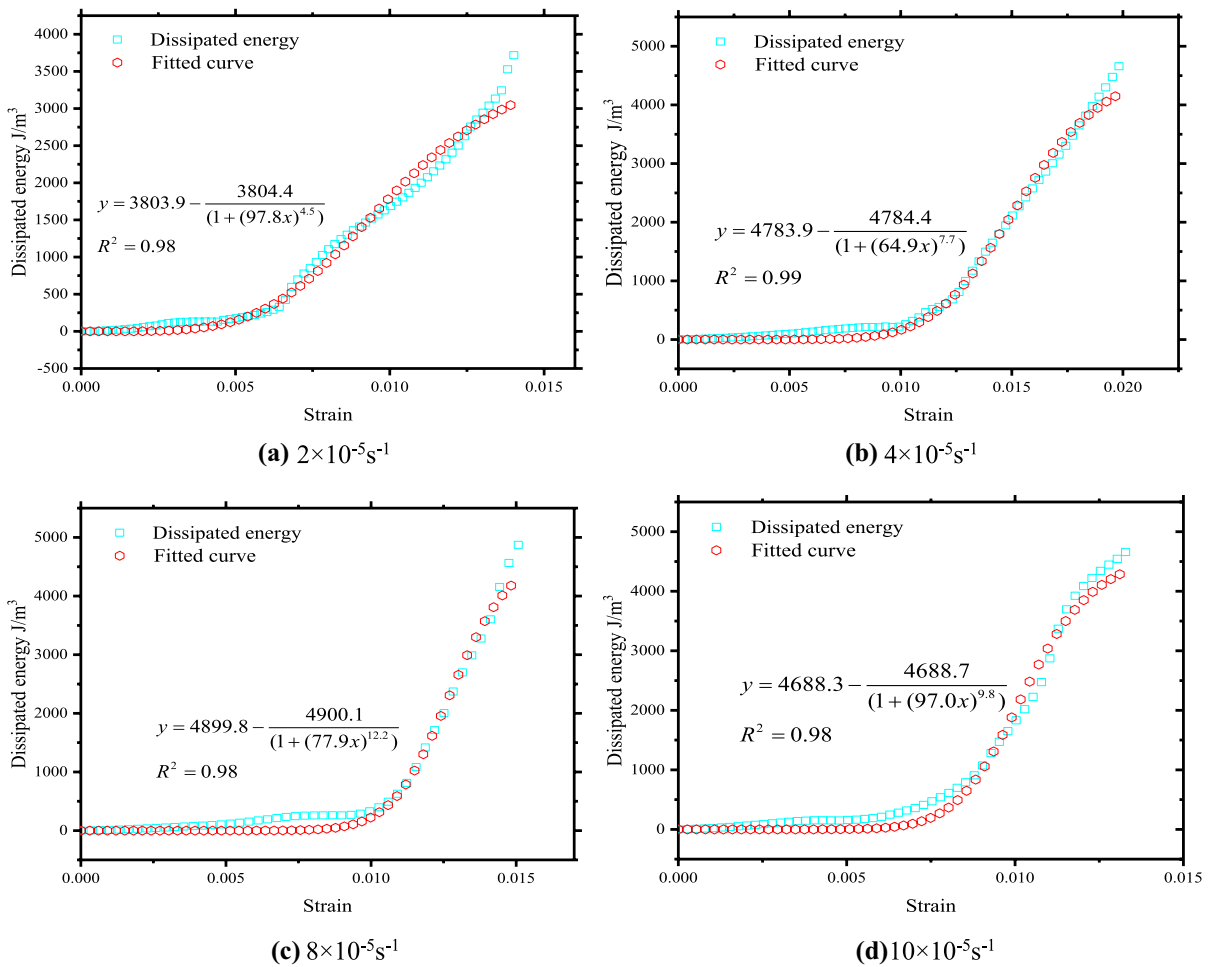


Fig. 8 Curve of dissipated energy versus strain at different strain-rates

stress, σ_c is the peak stress, and a , b , and c are material-related constants.

Substituting (7) into (6) in the uniaxial compression state, the mechanical instantiation equation based on the SIR model with damage parameters can be obtained, as shown by the following equation:

$$D = \begin{cases} 0 & \varepsilon \leq \gamma \\ 1 - \exp \left[-\frac{1}{2\Omega} \int c \left(e^{b\varepsilon/\varepsilon_c} - e^{a\varepsilon/\varepsilon_c} \right) \sigma_c d\varepsilon \right] & \varepsilon > \gamma \end{cases} \quad (8)$$

where a/ε_c , b/ε_c , and $c\sigma_c$ are constants and can be defined as a_1 , b_1 , and c_1 , respectively. With the constitutive equation substituted into the boundary conditions, the damage dissipation energy is obtained by calculating the following equation:

$$\Omega = \frac{c_1 \left(e^{b_1\varepsilon_c} - e^{a_1\varepsilon_c} \right) \left(b_1 e^{b_1\varepsilon_c} - a_1 e^{a_1\varepsilon_c} \right)}{2\varepsilon_c} \quad (9)$$

The greater the damage dissipation energy is, the more energy input is required for damage to occur, and the more difficult it is for damage to occur. Due to space limitations, damage evolution analysis was performed on the most representative specimens of each group. Figure 9 shows the damage values versus strain for the CPB under different strain rates.

As Fig. 9 shows, the damage evolution curves of the CPB at different strain rates were all in the shape of an “S,” indicating that the compression damage to the CPB under different strain rates was of the same type. According to the growth law of

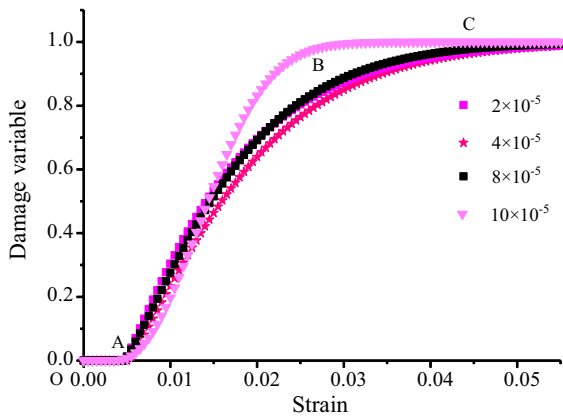


Fig. 9 Damage values versus strain for CPB under different strain rates

the damage evolution curve of the CPB, the energy damage evolution process of the CPB damaged by compression can be divided into three stages:

- Slow-growth damage phase (OA). At this time, the stress value and dissipation and elastic energies of the CPB are small, and the primary cracks inside the CPB are compressed and dense, corresponding to practically zero damage variables.
- Damage stabilization and accelerated growth phase (AB). The total strain energy absorbed by the CPB during this phase is mainly stored as elastic energy within the CPB. The damage evolution curve of the CPB shows that with continuous loading, the CPB is in the elastic deformation phase, still produces damage, and shows a steady growth trend. The dissipation energy of the CPB shows a clear increasing trend. In addition, the strain softening mechanism of the CPB starts to increase within this phase, and the damage value D starts to increase rapidly.
- Damage growth rate slowdown phase (BC). During this phase, the CPB no longer absorbs strain energy, and the rapid increase in energy consumption value causes the CPB to lose strength due to increased damage. When the energy consumption value reaches the extreme value, the damage value reaches its maximum value, and the CPB forms monolithic damage.

4 Conclusions

In this study, the damage evolution process of CPB was investigated by conducting uniaxial loading tests with different strain rates and analyzing their strain field and energy evolution curves through a combination of AE and DIC in situ monitoring. The results of the study can be described as follows.

- The phenomenon of a critical strain rate exists for low-strength CPB. Below the critical strain rate, the increase in the strain rate has a significant strengthening effect on the compressive strength of CPB, and vice versa. This produces a deterioration effect, which is significantly different from that of hard brittle rocks.
- The increase in the strain rate has a significant effect on the strain field evolution pattern of CPB, and the transfer of the strain concentration area of the specimens during loading has a strain rate effect.
- The growth of the total energy consumption and axial strain of CPB generally follows the logistic model. The energy consumption required to achieve the same axial deformation tends to increase and then decrease with an increase in the strain rate.
- The damage evolution curves of CPB at different strain rates are all “S”-shaped and can be divided into phases of slow-growth damage, damage stabilization and accelerated growth, and damage growth rate slowdown.

Acknowledgements The study has been supported by the National Natural Science Foundation (No. 51764013), by Training Plan for Academic and Technical Leaders of Major Disciplines of Jiangxi Province (20204BCJ22005), by China Postdoctoral Science Foundation funded project (Grant No. 2019M652277), by Natural Science Youth Foundation Key Projects of Jiangxi Province of China (Grant No.20192ACBL21014).

Funding National Natural Science Foundation of China, No. 51764013, Kang Zhao, Major Discipline Academic and Technical Leaders Training Program of Jiangxi Province, 20204BCJ22005, Kang Zhao, Postdoctoral Research Foundation of China, Grant No. 2019M652277, Kang Zhao, Youth Science Foundation of Jiangxi Province, Grant No.20192ACBL21014, Kang Zhao

Declarations

Conflict of interest No conflict of interest exists in the submission of this manuscript, and manuscript is approved by all authors for publication. I would like to declare on behalf of my co-authors that the work described was original research that has not been published previously, and not under consideration for publication elsewhere, in whole or in part. All the authors listed have approved the manuscript that is enclosed.

References

- Argane R, Benzaazoua M, Hakkou R, Bouamrane A (2015) Reuse of base-metal tailings as aggregates for rendering mortars: assessment of immobilization performances and environmental behavior. *Constr Build Mater* 96:296–306
- Benzaazoua M, Fall M, Belem T (2004) A contribution to understanding the hardening process of cemented paste-fill. *Miner Eng* 17(2):141–152
- Cao S, Yilmaz E, Song W, Yilmaz E, Xue G (2019) Loading rate effect on uniaxial compressive strength behavior and acoustic emission properties of cemented tailings backfill. *Construct Build Mater* 213:313–324
- Cao S, Yilmaz E, Yin Z, Xue G, Song W, Sun L (2020) CT scanning of internal crack mechanism and strength behavior of cement-fiber-tailings matrix composites. *Cem Concr Compos* 116:103865
- Carabba L, Pirskawetz S, Krüger S, Gluth GJ, Bignozzi MC (2019) Acoustic emission study of heat-induced cracking in fly ash-based alkali-activated pastes and lightweight mortars. *Cem Concr Compos* 102:145–156
- Chen Q, Zhang Q, Fourie A, Xin C (2017) Utilization of phosphogypsum and phosphate tailings for cemented paste backfill. *J Environ Manag* 201:19–27
- Chen QS, Zhang Q, Qi C, Fourie A, Xiao C (2018) Recycling phosphogypsum and construction demolition waste for cemented paste backfill and its environmental impact. *J Clean Prod* 186:418–429
- Cheng AP, Dai SY, Zhang YS (2019) Study on size effect of damage evolution of cemented backfill. *Chin J Rock Mech Eng* 38(S1):3053–3060
- Cihangir F, Ercikdi B, Kesimal A, Deveci H, Erdemir F (2015) Paste backfill of high-sulphide mill tailings using alkali-activated blast furnace slag: effect of activator nature concentration and slag properties. *Miner Eng* 83:117–127
- Comley K, Fleck N (2012) The compressive response of porcine adipose tissue from low to high strain-rate. *Int J Impact Eng* 46:1–10
- Crammond G, Boyd SW, Dulieu-Barton JM (2013) Use of DIC for the failure analysis of complex composite structures
- Dai S, Liu X, Nawnit K (2019) Experimental study on the fracture process zone characteristics in concrete utilizing DIC and AE methods. *Appl Sci* 9(7):1346
- Das AK, Leung CK (2019) Power spectral entropy of acoustic emission signal as a new damage indicator to identify the operating regime of strain hardening cementitious composites. *Cem Concr Compos* 104:103409
- Dzaye ED, De Schutter G, Aggelis DG (2020) Monitoring early-age acoustic emission of cement paste and fly ash paste. *Cem Concr Res* 129:105964
- Featherston CA (2012) Geometric imperfection sensitivity of curved panels under combined compression and in-plane bending—a study using adaptive meshing and DIC. *Strain* 48(4):286–295
- Felekoğlu B, Tosun K, Baradan B (2009) Effects of fibre type and matrix structure on the mechanical performance of self-compacting micro-concrete composites. *Cem Concr Res* 39(11):1023–1032
- Fu J, Wang J, Song W (2020) Damage constitutive model and strength criterion of cemented paste backfill based on layered effect considerations. *J Market Res* 9(3):6073–6084
- Gilat A, Goldberg RK, Roberts GD (2007) Strain-rate sensitivity of epoxy resin in tensile and shear loading. *J Aerosp Eng* 20(2):75–89
- Golewski GL (2019) Measurement of fracture mechanics parameters of concrete containing fly ash thanks to use of digital image correlation (DIC) method. *Measurement* 135:96–105
- Gong F, Shi R, Xu L (2022) Linear energy storage and dissipation laws of concrete under uniaxial compression at different ages. *Constr Build Mater* 318:125963
- Griffiths J, Lowrie D, Williams J (2000) An age-structured model for the AIDS epidemic. *Eur J Oper Res* 124(1):1–14
- Hagara M, Trebuña F, Huňady R, Kalina M, Schrötter M (2012) Experimental identification of modal parameters of thin metal sheets by using of DIC. *Procedia Eng* 48:180–188
- He Z, Zhao K, Yan Y, Ning F, Zhou Y, Song Y (2021) Mechanical response and acoustic emission characteristics of cement paste backfill and rock combination. *Constr Build Mater* 288:123119
- Hou Y, Yin S, Cao Y, Dai C (2020) Research on damage and energy dissipation characteristics of cemented backfill under different loading rates. *J Hunan Univ (natural Sciences)* 47(08):108–117
- JGJ 55—2011 (2011) Specification for mix proportion design of ordinary concrete, China Architecture & Building Press, Beijing, pp 1–18
- Koupouli NJ, Belem T (2019) Direct shear tests on cemented paste backfill–rock wall and cemented paste backfill–backfill interfaces. *J Rock Mech Geotech Eng* 8(4):472–479
- Kourkoulis SK, Darmanis S, Papadogoulas A, Pasiou ED (2017) 3D-DIC in the service of orthopaedic surgery: comparative assessment of fixation techniques for acetabular fractures. *Eng Fract Mech* 183:125–146
- Lacidogna G, Piana G, Accornero F, Carpinteri A (2020) Multi-technique damage monitoring of concrete beams: acoustic emission, digital image correlation, dynamic identification. *Constr Build Mater* 242:118114
- Lee JH, Veysset D, Singer JP, Retsch M, Saini G, Pezeril T, Thomas EL (2012) High strain-rate deformation of layered nanocomposites. *Nat Commun* 3(1):1–9
- Lei R, Zhang Z, Berto F, Ranjith PG, Liu L (2020) Cracking process and acoustic emission characteristics of sandstone with two parallel filled-flaws under biaxial compression. *Eng Fract Mech* 237:107253

- Li YG, Jin LZ, Tan H (2016) Experiment of loading rate effect on mechanical characteristics of cemented filling body. *J Harbin Inst Technol* 48(9):49–53
- Liu L, Xin J, Huan C, Qi C, Zhou W, Song K (2020a) Pore and strength characteristics of cemented paste backfill using sulphide tailings: effect of sulphur content. *Constr Build Mater* 237:117452
- Liu L, Xin J, Qi C, Jia H, Song KI (2020b) Experimental investigation of mechanical, hydration, microstructure and electrical properties of cemented paste backfill. *Constr Build Mater* 263:120137
- Mahanta B, Tripathy A, Vishal V, Singh TN, Ranjith PG (2017) Effects of strain-rate on fracture toughness and energy release rate of gas shales. *Eng Geo* 218:39–49
- Pierron F, Sutton MA, Tiwari V (2011) Ultra high speed DIC and virtual fields method analysis of a three point bending impact test on an aluminium bar. *Exp Mech* 51(4):537–563
- Qi C, Fourie A (2019) Cemented paste backfill for mineral tailings management: review and future perspectives. *Miner Eng* 144:106025
- Qi C, Fourie A, Chen Q, Zhang Q (2018a) A strength prediction model using artificial intelligence for recycling waste tailings as cemented paste backfill. *J Clean Prod* 183:566–578
- Qi C, Fourie A, Chen Q (2018b) Neural network and particle swarm optimization for predicting the unconfined compressive strength of cemented paste backfill. *Constr Build Mater* 159:473–478
- Reu PL, Toussaint E, Jones E, Bruck HA, Iadicola M, Balcaen R, Simonsen M (2018) DIC challenge: developing images and guidelines for evaluating accuracy and resolution of 2D analyses. *Exp Mech* 58(7):1067–1099
- Rokoš O, Hoefnagels JPM, Peerlings RHH, Geers MGD (2018) On micromechanical parameter identification with integrated DIC and the role of accuracy in kinematic boundary conditions. *Int J Solids Struct* 146:241–259
- Rosenthal I, Stern A, Frage N (2017) Strain-rate sensitivity and fracture mechanism of AlSi10Mg parts produced by selective laser melting. *Mater Sci Eng, A* 682:509–517
- Roux-Langlois C, Gravouil A, Baietto MC, Réthoré J, Mathieu F, Hild F, Roux S (2015) DIC identification and X-FEM simulation of fatigue crack growth based on the Williams' series. *Int J Solids Struct* 53:38–47
- Stoddart EP, Byfield MP, Davison JB, Tyas A (2013) Strain-rate dependent component based connection modelling for use in non-linear dynamic progressive collapse analysis. *Eng Struct* 55:35–43
- Sun Q, Tian S, Sun Q, Li B, Cai C, Xia Y, Wei X, Mu Q (2019) Preparation and microstructure of fly ash geopolymer paste backfill material. *J Clean Prod* 225:376–390
- Thomson DM, Cui H, Erice B, Hoffmann J, Wiegand J, Petrinic N (2017) Experimental and numerical study of strain-rate effects on the IFF fracture angle using a new efficient implementation of Puck's criterion. *Compos Struct* 181:325–335
- Xia Y, Zhu J, Zhou Q (2015) Verification of a multiple-machine program for material testing from quasi-static to high strain-rate. *Int J Impact Eng* 86:284–294
- Xie HP, Ju Y, Li LY (2005) Rock strength and overall failure criterion based on energy dissipation and release principle. *Chin J Rock Mech Eng* 24(17):3003–3010
- Xu WB, Du JH, Song WD (2013) Experiment on the mechanism of consolidating backfill body of extra-fine grain unclassified tailings and cementitious materials. *Rock Soil Mech* 34(8):2295–2302
- Xue G, Yilmaz E, Song W, Cao S (2019a) Mechanical, flexural and microstructural properties of cement-tailings matrix composites: effects of fiber type and dosage. *Compos B Eng* 172:131–142
- Xue G, Yilmaz E, Song W, Cao S (2019b) Analysis of internal structure behavior of fiber reinforced cement-tailings matrix composites through X-ray computed tomography. *Compos B Eng* 175:107091
- Yashar A, Ferguson N, Tehrani MG (2017) Measurement of rotating beam vibration using optical (DIC) techniques. *Procedia Eng* 199:477–482
- Yilmaz E, Belem T, Benzaazoua M (2013) Study of physico-chemical and mechanical characteristics of consolidated and unconsolidated cemented paste backfills. *Min Resour Manag* 29(1):81–100
- Zhang S, Ren F, Guo Z, Qiu J, Ding H (2020) Strength and deformation behavior of cemented foam backfill in sub-zero environment. *J Market Res* 9(4):9219–9231
- Zhao K, Yu X, Zhu ST, Zhou Y, Wang Q, Wang JQ (2020a) Acoustic emission investigation of cemented paste backfill prepared with tantalum-niobium tailings. *Constr Build Mater* 237:117523
- Zhao K, Yu X, Zhou Y, Wang Q, Wang J, Hao J (2020b) Energy evolution of brittle granite under different loading rates. *Int J Rock Mech Min Sci* 132:104392
- Zhao K, Zhou Y, Yu X, Yan Y, Song Y, Wang J, Guo X (2021) Dynamic prediction model of overburden settlement in deep mining areas based on space-time relationship. *Nat Resour Res* 30(5):3839–3852
- Zhao K, Huang M, Zhou Y, Yan Y, Wan W, Ning F, Wang J (2022) Synergistic deformation in a combination of cemented paste backfill and rocks. *Constr Build Mater* 317:125943
- Zhou J, Liu Y, Li Z (2014) Damage evolution of structured soil based on energy method. *Chin J Geotech Eng* 35(9):1689–1695
- Zhou Y, Yu X, Guo Z, Yan Y, Zhao K, Wang J, Zhu S (2021) On acoustic emission characteristics, initiation crack intensity, and damage evolution of cement-paste backfill under uniaxial compression. *Constr Build Mater* 269:121261
- Zhou Y, Yan Y, Zhao K, Yu X, Song Y, Wang J, Suo T (2021) Study of the effect of loading modes on the acoustic emission fractal and damage characteristics of cemented paste backfill. *Constr Build Mater* 277:122311
- Zhu WC, Niu LL, Li SH, Xu ZH (2015) Dynamic Brazilian test of rock under intermediate strain-rate: pendulum hammer-driven SHPB test and numerical simulation. *Rock Mech Rock Eng* 48(5):1867–1881

Publisher's Note Springer Nature remains neutral with regard to jurisdictional claims in published maps and institutional affiliations.

Springer Nature or its licensor holds exclusive rights to this article under a publishing agreement with the author(s) or other rightsholder(s); author self-archiving of the accepted manuscript version of this article is solely governed by the terms of such publishing agreement and applicable law.